JACS
JOURNAL OF THE AMERICAN CHEMICAL SOCIETY
Article
pubs.acs.org/JACS

Uniform Doping of Metal Oxide Nanowires Using Solid State Diffusion

Joaquin Resasco,[†] Neil P. Dasgupta,[‡,§] Josep Roque Rosell,[∥] Jinghua Guo,[∥] and Peidong Yang*[,‡,⊥]

[†]Department of Chemical Engineering and [‡]Department of Chemistry, University of California, Berkeley, California 94720, United States

[§]Department of Mechanical Engineering, University of Michigan, Ann Arbor, Michigan 48109, United States

[∥]Advanced Light Source, Lawrence Berkeley National Laboratory, Berkeley, California 94720, United States

[⊥]Materials Sciences Division, Lawrence Berkeley National Laboratory, Berkeley, California 94720, United States

Supporting Information

ABSTRACT: The synthesis of one-dimensional nanostructures with specific properties is often hindered by difficulty in tuning the material composition without sacrificing morphology and material quality. Here, we present a simple solid state diffusion method utilizing atomic layer deposition to controllably alter the composition of metal oxide nanowires. This compositional control allows for modification of the optical, electronic, and electrochemical properties of the semiconductor nanowires. Using this method and a novel process for manganese oxide atomic layer deposition, we produced manganese-doped rutile TiO_2 nanowires and investigated their structural and photoelectrochemical properties. A homogeneous incorporation of the Mn dopant into the rutile lattice was observed, and the local chemical environment of the Mn was determined using X-ray absorption spectroscopy. The doping process resulted in a tunable enhancement in the electrocatalytic activity for water oxidation, demonstrating that this simple and general method can be used to control the properties of one-dimensional nanostructures for use in a variety of applications including solar-to-fuel generation.

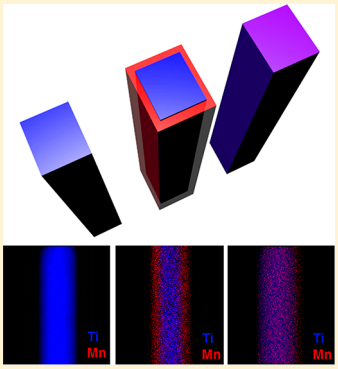

INTRODUCTION

One-dimensional nanostructured materials, such as nanorods or nanowires, exhibit unique properties that can be exploited in a diverse range of fields including photonics, energy conversion, and photoelectrochemistry.[1] In particular, one-dimensional semiconductor nanostructures are beneficial for use in photoelectrochemistry applications due to the large electrochemically available surface area afforded by their morphology, the decoupling of light absorption and minority carrier diffusion lengths for efficient charge collection and separation, and enhanced light scattering and trapping in vertical arrays.[2−5]

A variety of methods have been developed for synthesizing one-dimensional nanostructures including the vapor−liquid−solid,[6,7] vapor−solid,[8] solution−liquid−solid,[9] and hydrothermal methods.[10] However, synthesizing ternary or other complex one-dimensional nanostructures with compositional tunability, while maintaining control over the material quality and morphology remains challenging using traditional synthesis approaches. The simplest method for synthesizing bulk multinary compound solids is the solid state diffusion method, where reactants are mixed and heated to allow a diffusive transformation to the thermodynamically favored state. However, adapting this technique to one-dimensional nanostructures requires a technique to uniformly coat their surfaces with precise control of material loading. One technique that meets this requirement is atomic layer deposition (ALD).[11] ALD is a modified form of chemical vapor deposition (CVD) based on sequential, self-limiting surface reactions. Because of the saturation of the substrate surface with the reactant species after each half-cycle, highly conformal films can be deposited on high aspect ratio structures with subnanometer control of film thickness. This technique has been previously demonstrated to precisely tune the optical and electrochemical properties of nanowires by fabrication of uniform core−shell structures.[12,13] Here we demonstrate that a solid state diffusion process for one-dimensional nanostructures can be achieved using ALD to precisely control the surface coating thickness, which is followed by a post annealing step. This approach provides a general method for producing doped or ternary metal oxide nanostructures with compositional control while maintaining the desired morphology.

In this study, we demonstrate the compositional control afforded by this method and show its utility for photoelectrochemical water splitting. TiO_2 has been the most widely studied material in this field since Fujishima and Honda's first demonstration of unassisted solar water splitting.[14] Although the wide band gap of TiO_2 limits the achievable photocurrent due to the limited number of solar photons in the ultraviolet range, transition metal doping of TiO_2 can lead to visible light absorption, potentially increasing the maximum achievable efficiency.[15−17]

Received: June 7, 2014
Published: July 15, 2014

Additionally, theoretical and experimental investigations have shown that transition metal doping of TiO_2, particularly with Mn and Cr, increases the catalytic activity for the oxygen evolution reaction (OER).[18−20]

Changing the catalytic activity in this way relies on the ability to introduce the dopants without modifying the original crystal structure, such that the binding strength of the surface to the reaction intermediates can be precisely altered.

This conversion chemistry approach provides a high degree of synthetic control, allowing for the study of the effect of changes in composition on the catalytic activity. We utilize this method to produce Mn-doped TiO_2 nanowire arrays and study their photoelectrochemical properties. We further demonstrate the generality of this method using other material compositions.

EXPERIMENTAL SECTION

Synthesis of Titanium Dioxide Nanowire Arrays. Titanium dioxide (TiO_2) nanowires were synthesized by a hydrothermal method.[10] In a typical synthesis, 83 μL of titanium isopropoxide (Sigma-Aldrich) was mixed with 5 mL of 6 M hydrochloric acid (Sigma-Aldrich) in a 40 mL telfon vessel. A fluorine-doped tin oxide (FTO) coated quartz substrate was angled against the wall of the Teflon vessel such that the FTO surface was facing down. The Teflon vessel was loaded in a stainless steel autoclave and heated to 210 °C for 150 min. After cooling, the substrates were thoroughly rinsed in deionized water, yielding single crystalline rutile-TiO_2 nanowire arrays. For higher temperature annealing, a TiO_2 thin film (∼30 nm) was deposited on a quartz substrate as a seeding layer for nanowire growth.

Atomic Layer Deposition (ALD). Deposition of MnO_x thin films was performed in a customized thermal ALD reactor. The precursors used for MnO_x deposition were Manganese bis(*N*,*N*′-diisopropylacetamidinate) (Dow) and water. The manganese precursor was held in a customized bubbler that allowed for pulsed doses using nitrogen as a delivery gas through the bubbler, which was maintained at 100 °C. The water source was maintained at room temperature. The substrate temperature for MnO_x deposition was 150 °C. Typical pulse times for the manganese precursor and water were 1.5 and 1.0 s, respectively. The precursors used for ZrO_2 deposition were tetrakis(dimethylamido) zirconium (Strem) and water. The zirconium precursor was held in a stainless steel cylinder maintained at 75 °C. The substrate temperature for ZrO_2 deposition was 225 °C. Typical pulse times for the zirconium precursor and water were 1.5 and 1.0 s, respectively. Nitrogen was used as a carrier and purge gas in both processes at a flow rate of 10 sccm.

Conversion Process. After the atomic layer deposition process, the nanowire substrates were loaded into the center of a 1-in. diameter quartz tube and heated in a tube furnace under an Ar atmosphere at 873−1273 K for 1−24 h.

Physical and Chemical Characterization. The morphology of the nanowire substrates was studied using scanning electron microscopy (SEM). SEM images were collected using a JEOL JSM 6340F field-emission SEM operating at 5 kV. Phase information was obtained using X-ray diffraction (XRD). XRD patterns were collected using a Bruker D8 Advance diffractometer with Cu Kα radiation. Individual nanowires were imaged by transmission electron microscopy (TEM) using a JEOL 2100-F field-emission analytical TEM operated at 200 kV equipped with an analytical pole piece, a high solid-angle EDS system, and a HAADF (high-angle annular dark field) scanning TEM (STEM) detector, as well as a Hitachi H-7650 TEM operating at 120 kV. Chemical information about the Mn dopant atoms was investigated using X-ray photoelectron spectroscopy (XPS) and X-ray absorption spectroscopy (XAS). XPS spectra were collected using a PHI 5400 X-ray Photoelectron Spectrometer equipped with a 4 kV Argon ion gun, with Al Kα radiation. The angle between the source and detector was 35°. The measurement chamber was maintained at 10^{-9} torr during measurement, and measurements were taken at a pass energy of 17.9 eV. All energies were calibrated to spurious carbon at 285.0 eV.

XAS spectra were collected on beamline 10.3.2 at the Advanced Light Source (ALS) with an electron energy of 1.9 GeV and an average current of 500 mA. The radiation was monochromated by a Si (111) double-crystal monochromator. The intensity of the incident X-ray was monitored by an N_2-filled ion chamber (I_0) in front of the sample. Fluorescence spectra were recorded using a seven-element Ge solid-state detector. The energy was calibrated using a glitch in the I_0 relative to the absorption edge of Mn foil. All spectra were collected at room temperature. Data reduction of XAS spectra was done using the commonly employed Athena software. Pre-edge and postedge contributions were subtracted, and results were normalized to the absorption edge step. Background removal in k-space was achieved using a five-domain cubic spline. Curve fitting was performed with Artemis and IFEFFIT software using ab initio-calculated phases and amplitudes from the program FEFF 8.2 (S2, S3). These ab initio phases and amplitudes were used in the EXAFS equation:

$$\chi(k) = S_0^2 \sum_j \frac{N_j}{kR_j^2} f_{\mathrm{eff}_j}(\pi, k, R_j) e^{-2\sigma_j^2 k^2} e^{-2R_j/\lambda_j(k)} \times \sin(2kR_j + \varphi_{ij}(k))$$

The neighboring atoms to the central atom are divided into *j* shells, with all atoms with the same atomic number and distance grouped into a single shell. Within each shell, the coordination number N_j denotes the number of neighboring atoms in shell *j* at a distance of R_j from the central atom. $f_{\mathrm{eff}_j}(\pi,k,R_j)$ is the ab initio amplitude function for shell *j*, and the Debye−Waller term $e^{-2\sigma_j^2 k^2}$ accounts for the damping due to static and thermal disorder in absorber−backscatterer distances. The mean free path term $e^{-2R_j/\lambda_j(k)}$ reflects losses due to inelastic scattering, where $\lambda_j(k)$ is the electron mean free path. The oscillations in the EXAFS spectrum are reflected in the sinusoidal term, $\sin(2kR_j + \phi_{ij}(k))$ where $\phi_{ij}(k)$ is the ab initio phase function for shell *j*. S_0^2 is an amplitude reduction factor due to shakeup/shake-off processes at the central atom. The EXAFS equation was used to fit the experimental data using S_0, R, and the Debye−Waller factor (σ^2) as variable parameters. N was taken as known for these crystalline materials. For the energy (eV) to wave vector (k, Å^{-1}) conversion, E_0 was defined as 6547.5 eV, and ΔE_0 was obtained in the fit. The optical absorption spectra were recorded using a UV−vis−NIR scanning spectrophotometer equipped with an integration sphere (Shimadzu UV-3101PC).

Electrochemical Characterization. Electrochemical activity and stability of the nanowire substrates were studied in a three-electrode electrochemical cell using a Bio-Logic potentiostat/galvanostat with a built-in electrochemical impedance spectroscopy (EIS) analyzer. All CVs were *iR*-compensated at 85% and measured in 1 M KOH electrolyte at room temperature, using a platinum wire counter electrode and a Hg/HgO reference electrode. The potential scale was calibrated to a reversible hydrogen electrode (RHE). A 300-W Xe lamp equipped with an air mass 1.5 G filter (Newport) was used as the light source. Prior to measurement, light intensity was standardized using a calibrated silicon photodiode.

RESULTS AND DISCUSSION

A novel method for ALD of manganese oxide was developed using a bis(isopropylacetamidinate)manganese precursor and water vapor as coreactants. Previously reported work on ALD of manganese oxide has typically relied on cyclopentadienyl precursors.[23−25] Amidinates are well suited for use as ALD precursors due to their high volatility, thermal stability, and reactivity, and have been successfully used for ALD and CVD of various transition metals and transition metal oxides.[26−28] To measure film thicknesses, ALD MnO_x was deposited on planar Si substrates and conformally coated on TiO_2 nanowires yielding core−shell nanowires. The film thicknesses on Si were measured using ellipsometry, and the thickness on the nanowires was measured using transmission electron microscopy (TEM). Two important characteristics of an ALD reaction are the saturation of the surface reaction after each precursor pulse, and a linear relationship between film thickness and number of cycles after a

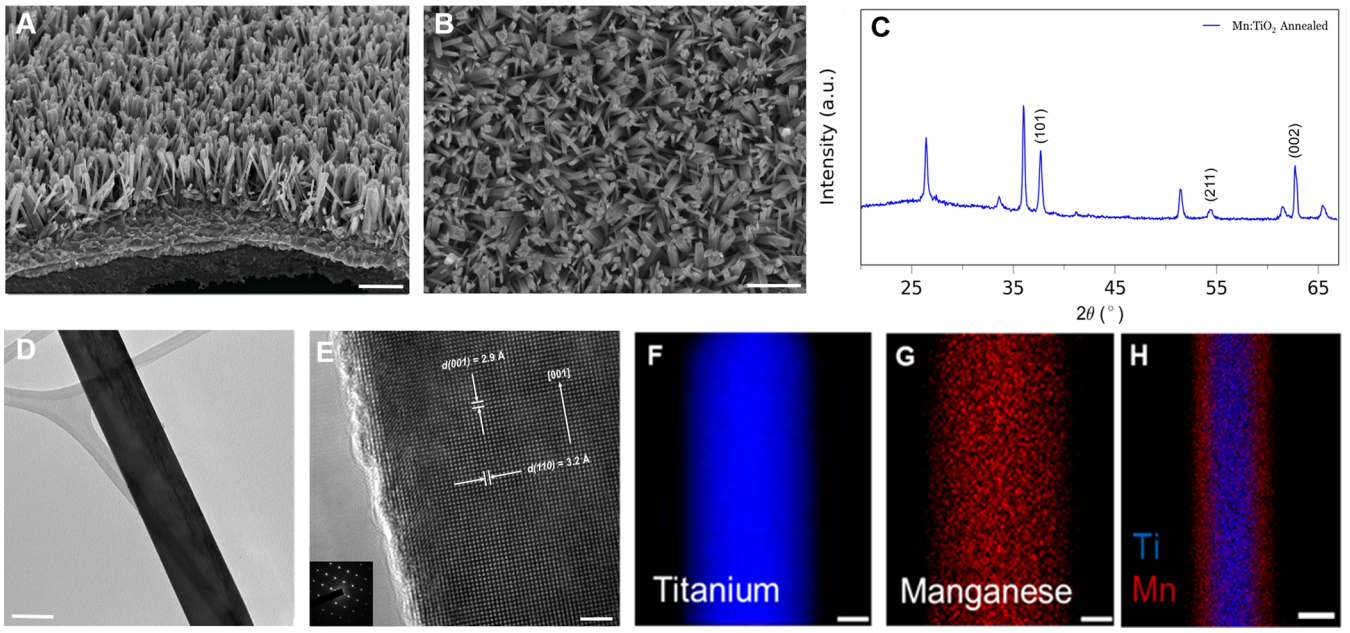

Figure 1. (A,B) 45° and top down SEM images of vertically aligned Mn:TiO_2 nanowire array, scale bar is 1 μm. (C) XRD pattern of converted nanowires showing only peaks for rutile TiO_2 and peaks corresponding to FTO substrate. Peaks for rutile TiO_2 are indicated. (D,E) TEM and HRTEM image of converted nanowire showing lattice spacing consistent with rutile TiO_2, scale bars are 100 and 2 nm, respectively. (F,G) STEM mode elemental maps of Mn and Ti in converted wire showing homogeneous incorporation of dopant; scale bars are 20 nm. (H) STEM mode elemental map of Mn and Ti in core−shell nanowire before annealing. Scale bar is 50 nm.

sufficient number of cycles. Saturating, linear growth was demonstrated indicating an ALD growth mode (Supporting Information). A growth rate of ∼1 Å/cycle was measured both on Si substrates and TiO_2 nanowires, with no thickness gradient along the nanowire length. Using XPS, no measurable carbon or nitrogen was observed in the spectrum following a 1 min Ar sputtering. Because the amidinate ligand contains carbon and nitrogen, the lack of any organic contamination in the film indicates that the ALD surface reaction was complete, and the ligands were completely substituted for by oxygen from the H_2O. Information about the ALD process, along with representative TEM images for core−shell nanowires can be found in the Supporting Information.

This ALD process was used to coat the TiO_2 nanowire arrays with manganese oxide, producing conformal core−shell nanowires with shell thicknesses that could be tuned with ∼1 Å precision (Figure 1h). The coated nanowire arrays were then annealed in an argon environment to facilitate diffusion of the manganese atoms into the rutile lattice, yielding Mn-doped TiO_2 nanowires. The diffusion mechanism and transient behavior is discussed in detail in the Supporting Information. The solid state diffusion process maintains the nanowire morphology as observed by scanning electron microscopy (SEM) with an average nanowire diameter ∼100 nm and length of ∼1.5 μm (Figure 1a,b). Energy dispersive X-ray spectroscopy (EDS) confirms the presence of Mn in the nanowire arrays and allows for quantification of the average Mn content as a function of number of ALD cycles. The average composition of Mn in the nanowire arrays can be precisely tuned by varying the shell thickness, and is in good agreement with calculated values for this nanowire geometry (Supporting Information). The concentration of Mn could not be extended above 10%, which is likely due to the solubility limit of Mn in TiO_2. XPS confirmed that the near surface composition of the nanowires is similar to the average composition in the core. The XRD pattern of the nanowire substrates after annealing only contains peaks corresponding to the rutile phase, with no MnO_x or $MnTiO_x$ ternary phases observed (Figure 1c). With annealing temperatures above 1223 K, the ternary phase $MnTiO_3$ was formed for doped samples with Mn atomic concentrations above 5%. These higher annealing temperatures resulted in axially segmented nanowires with epitaxial interfaces between $MnTiO_3$ and TiO_2 (Supporting Information).

To determine the distribution of the dopant atoms in the TiO_2 nanowires and their effect of the nanowire structure, the converted nanowires were further analyzed by TEM. TEM images of Mn-doped TiO_2 nanowires show no sign of a MnO_x shell after annealing, indicating that the conversion process proceeded to completion. High resolution TEM (HRTEM) analysis was used to investigate the microstructure of the doped nanowires and indicated that the nanowires remained single crystalline after growth. Using HRTEM, we observed lattice spacing consistent with rutile TiO_2 with the nanowire growth axis parallel to the [001] direction. To obtain a visualization of the distribution of the Mn atoms within the TiO_2 lattice, STEM mode EDS mapping was conducted. The elemental maps show a homogeneous incorporation of the Mn atoms, in contrast with the core−shell nanowire prior to annealing. Line scans across the diameter and length of the wire before and after annealing are shown in the Supporting Information, illustrating the conversion of the core−shell geometry into a homogeneous doped nanowire. To show the generality of the conversion chemistry approach, the method was also applied successfully to synthesize zirconium-doped TiO_2 using ALD of ZrO_2 as a dopant source. Elemental maps for the Zr-doped wires can be seen in the Supporting Information. The maximum achievable dopant concentration using Zr was found to be significantly lower than that observed using Mn, presumably due to the lower solubility of Zr in TiO_2. No signal from Sn or F was observed by EDS in any of the nanowires tested. The results of the TEM and XRD analyses suggest that this conversion process allows for controlled

dx.doi.org/10.1021/ja505734s | J. Am. Chem. Soc. 2014, 136, 10521−10526

homogeneous doping of the TiO_2 nanowires while maintaining the original crystal structure. For further insight into the chemical environment and oxidation state of the Mn dopant atoms within the TiO_2 lattice, XPS and X-ray absorption spectroscopy (XANES, EXAFS) were used.

XPS was used to study the oxidation state of Mn before and after the conversion process. Assignment of the oxidation state of Mn is not generally possible from the photoelectron peak positions alone, as the binding energies for different oxidation states are quite similar. However, previous studies have shown that comparison of the relative peak position of the $2p_{1/2}$ satellite to its parent peak and the magnitude of the 3s multiplet splitting can be used to determine the oxidation state of manganese.[29−31] The Mn^{2+} oxidation state has a clear satellite peak approximately 6 eV from the parent $2p_{1/2}$, which is absent in the higher oxidation states. Oxides in the higher oxidation states have a weaker peak near 10−11 eV from the $2p_{1/2}$ peak. The multiplet splitting of the 3s peak is also dependent on the oxidation state. An increased oxidation state corresponds to fewer unpaired 3p electrons, leading to a weaker coupling with the unpaired core-level electron formed in the photoionization process, which results in a smaller multiplet splitting. The as deposited film was found to have a $\Delta 2p_{1/2}$ of 10.75 eV and a Δ3s of 5.7 eV indicating an average oxidation state between Mn^{3+} and Mn^{4+} as seen in Figure 2. As the metallorganic precursor contains Mn^{2+} cations and surface oxidation of MnO is well-known, it is possible that the ALD film deposits in a lower oxidation state and is oxidized in ambient conditions. After annealing, the $\Delta 2p_{1/2}$ was reduced to 6.2 eV and a Δ3s of 6.0 eV, matching that of the MnO phase. The annealing process therefore reduces the Mn from a mixed $Mn^{3+/4+}$ valence to a Mn2+ oxidation state, possibly due to the formation of oxygen vacancies in the Ar environment. The Ti 2p region of the undoped and doped samples was also investigated, and no change was observed in the binding energies or peak structure (Supporting Information).

For further confirmation of the oxidation state of the Mn dopants and determination of their chemical environment within the TiO_2 lattice, near edge and extended X-ray absorption fine structure (XANES, EXAFS) spectroscopy was conducted on the Mn K edge and Ti K edge. The absorption edge position was used to determine the oxidation state, with the position being taken as point of inflection in the absorption edge. The oxidation state was compared with reference samples of Mn^0, Mn^{2+}, Mn^{3+}, and Mn^{4+}. The XANES spectra, as seen in Figure 2, shows the Mn edge energy is 6551.0 eV in the as deposited film indicating the Mn atoms are in a mixed $Mn^{3+/4+}$ oxidation state. The Mn edge energy moves to 6547.5 eV after annealing in Ar corresponding to a reduction of the oxidation state to Mn^{2+}, in agreement with the results of the XPS study. A principal component analysis was performed to fit the experimental spectra with a linear combination of manganese oxide reference samples. The as deposited sample could be described by a linear combination of ~50% Mn_2O_3 and 50% MnO_2, indicating that the chemical environment of the manganese atoms in the as deposited sample is similar to that in the manganese oxide phases. However, the fine structure of the annealed sample could not be reproduced by the reference spectra, indicating the chemical environment of the Mn in the TiO_2 lattice is quite different to that of the manganese oxide phases, in accordance with the results of the XRD and TEM studies.

The Ti K edge EXAFS spectrum was taken for both the undoped and doped nanowire samples. The nanowires have the rutile structure, in which each Ti atom is octahedrally coordinated and bonded to 6 O atoms. The 6 O atoms are found at two distinct distances of 1.93 and 2.0 Å. The next nearest paths are the Ti−Ti path between the Ti atom at the body center of a rectangular prism and the eight Ti atoms occupying the vertices of the rectangular prism. The effect of the transition metal substitution for Ti should be therefore be seen in the structure of the second and third peaks. However, due to the low concentration of the dopant, the spectra are nearly unchanged, indicating a preservation of the original rutile lattice and a chemical environment for the average Ti atom that is not significantly perturbed by the presence of the Mn dopant. As it is assumed that Mn acts as a substitutional dopant for Ti, the EXAFS spectrum of the dopant taken on the Mn K edge can be qualitatively compared to the Ti K edge EXAFS spectrum, shown in Figure 2. The spectra show clear similarities although the paths dominated by the Mn−O and Mn−Ti bonds appear longer, indicating a structural distortion caused by the larger ionic radius of the Mn^{2+} ion. A fitting of the experimental spectrum was performed using ab initio FEFF calculations, to extract quantitative structural parameters.[21,22] The structure model used was a rutile cluster

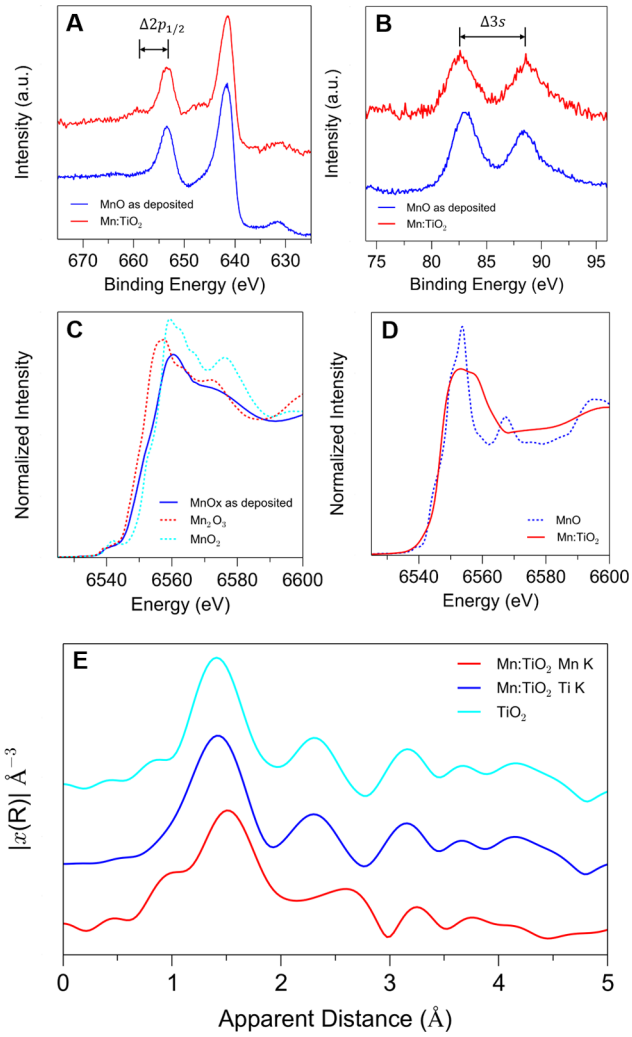

Figure 2. (A,B) XPS spectra of the Mn 2p and 3s regions, indicating the satellite peak distance in the 2p region and the 3s multiplet peak splitting. (C,D) Mn K edge XANES spectra with reference spectra showing the change in Mn valence and fine structure change on annealing. (E) Mn K edge and Ti K edge Fourier transform EXAFS spectra showing dopant coordination environment.

dx.doi.org/10.1021/ja505734s | J. Am. Chem. Soc. 2014, 136, 10521−10526

with the core atom being replaced with Mn. This structural model provides a good fit to the experimental spectrum, and the bond lengths are observed to be extended, with the Mn−O bonds being 2.03 and 2.15 Å, similar to the Mn−O bond length seen in the Mn^{2+} oxide, and the Mn−Ti path being 3.30 Å.

To evaluate the impact of the Mn doping process on the properties of the nanowires, electrochemical measurements were performed. The electrocatalytic activity of the nanowire substrates for the OER was evaluated across the entire compositional range investigated using cyclic voltammetry in a standard 3 electrode setup. The relevant figure of merit used for evaluation of electrocatalytic activity for solar water splitting devices is the overpotential required to achieve a current density of 10 mA cm^{-2}.[32] The difference in catalytic activities between different surfaces for the OER is determined by the O* adsorption energy.[33] Rutile TiO_2 lies on the right side of the OER activity volcano, indicating the O* binding is too weak. The introduction of the dopant leads to a stronger interaction between the adsorbate and the surface, resulting in a binding energy nearer the maximum of the activity volcano. The ability to alter the composition while maintaining the original crystal structure allows for access to intermediate binding energies between those of the undoped surface and the dopant in its oxide phase.[18] The overpotential was reduced for all concentrations measured for the converted nanowire substrates (Figure 3a).

The lowest overpotential was measured for Mn:TiO_2 prepared from 50 cycles of ALD, denoted 50× Mn:TiO_2, corresponding to a doping concentration of ∼6%, similar to the dopant concentration used for the computational studies of Nørskov and coworkers.[18] It is possible that at higher Mn concentrations the surface becomes too strongly binding. The overpotential required was 0.5 V, or a potential of 1.73 V versus the reversible hydrogen electrode. This value is comparable to previously reported values of 1.77 and 1.84 V for MnO_x electrocatalysts and ∼1.55−1.65 V for high performing electrodeposited catalysts.[23,32,34] The improvement observed here is also in agreement with previous studies on transition metal-doped TiO_2. The improvement in activity for ∼2% dopant concentration relative to the undoped TiO_2 is comparable to that found by Liu et al, although the current density in this study was limited by the small electrochemically accessible surface area of the submonolayer films.[20] The short-term stability of these samples was measured using chronopotentiometry. The catalyst material was held at a constant current density of 10 mA cm^{-2} per geometric area for 2 h while the potential needed to maintain this current density was measured (Figure 3b). The potential at 2 h increased to ∼1.8 V, indicating the catalyst is relatively stable, in contrast to MnO_x based catalysts, which form MnO_4^- soluble species and dissolve in alkaline conditions and under large applied potentials.[35]

Historically, a variety of transition metals have been explored as dopants in modifying the electronic structure of TiO_2 to improve its visible light photocatalytic activity.[15−17] Previous theoretical studies show that doping TiO_2 with manganese introduces an occupied mid gap state which is very localized and primarily comprised of the Mn t_{2g} orbitals. The visible light absorption in this material is a charge transfer from the dopant mid gap state to the conduction band or an acceptor transition from the valence band to the impurity band.[15] We observe that the doped samples are yellow-brown, departing from the white color of the undoped product. Consequently the light absorption of the Mn-doped TiO_2 nanowires extends from the ultraviolet into the visible range as an extended tail, potentially widening the usable range for photocarrier generation for driving the water

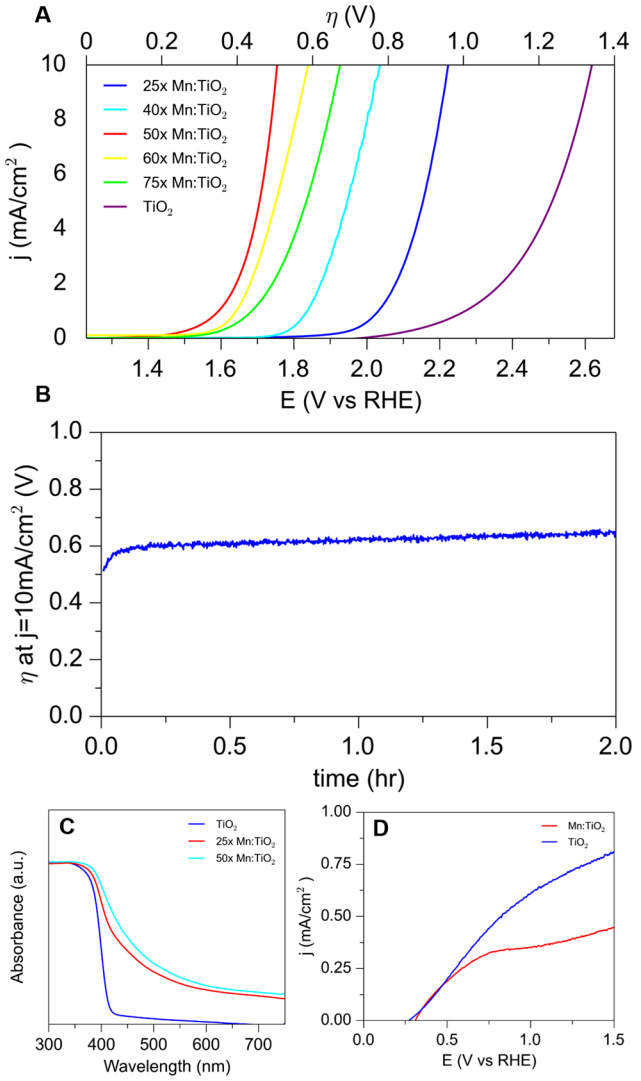

Figure 3. (A) Voltammograms of OER activity for doped and undoped nanowire samples with overpotential required to achieve a benchmark current density of 10 mA/cm^{-2} based on geometric surface area. 25× denotes a sample prepared from 25 cycles of MnO_x ALD. (B) Short-term stability test using controlled current electrolysis at 10 mA/cm^{-2} based on geometric surface area. (C) UV−visible absorption spectra of doped and undoped nanowire samples. (D) Photoelectrochemical performance of undoped and doped nanowire samples using 50× Mn:TiO_2.

oxidation reaction. (Figure 3c) It is important to note that the band edge position of the TiO_2 is unchanged, indicating that the tail in the visible range derives mainly from low energy excitations. The mid gap states introduced by the Mn impurity are predicted to be very localized, with little carrier mobility, and could possibly act as recombination centers. The photoelectrochemical performance of the doped TiO_2 films was measured in a 3 electrode set up under simulated solar illumination to determine the effect of the Mn dopant on the photoreactivity. The maximum photocurrent achieved from the doped devices was found to be reduced relative to that of the undoped devices, possibly indicating that the mid gap states formed by the transition metal dopant are acting as recombination centers. (Figure 3d) Although the transition metal doping process allows for visible light absorption, efficient charge collection is required to increase the obtainable photocurrent. This conversion chem-

dx.doi.org/10.1021/ja505734s | J. Am. Chem. Soc. 2014, 136, 10521−10526

istry approach could potentially be applied in such a way that the electronic structure of the light absorber is not negatively affected. This could include the synthesis of ternary metal oxide light absorbers or doping in which the impurity band formed connects with the valence or conduction band allowing for charge carrier extraction. Additionally the ability to precisely tune the composition of mixed metal oxides while maintaining a desired morphology has promise for the development of OER catalysts as demonstrated in this work.

We have developed a simple and general synthetic method for rationally designing complex metal oxide nanostructures, and demonstrated a novel process for atomic layer deposition of manganese oxide. In this study, we show the utility of this method by investigating the electrocatalytic, optical, and photoelectrochemical properties of Mn-doped TiO_2 nanowires as a model system. The Mn dopants are homogeneously incorporated in the rutile TiO_2 lattice without the formation of extraneous crystalline phases. These nanowires show promising electrocatalytic activity for water oxidation, but photoelectrochemical performance of the doped nanowire arrays is negatively affected, possibly owing to the introduction of an impurity band in the band gap of TiO_2. We further demonstrate the generality of this method by extending it to a second compositional system. Further studies could utilize this simple conversion chemistry approach to investigate functional complex metal oxide nanostructures, such as ternary metal oxide light absorbers or mixed metal oxides for water oxidation electrocatalysis.

■ ASSOCIATED CONTENT

Supporting Information

Experimental details, additional information about the ALD process, information about spectroscopic measurements, and mechanistic information on the diffusion process. Includes Figure S1−S13 and Table S1−S2. This material is available free of charge via the Internet at http://pubs.acs.org.

■ AUTHOR INFORMATION

Corresponding Author

p_yang@berkeley.edu

Notes

The authors declare no competing financial interest.

■ ACKNOWLEDGMENTS

This work was supported by the Director, Office of Science, Office of Basic Energy Sciences, Materials Sciences and Engineering Division, of the U.S. Department of Energy under Contract No. DE-AC02-05CH11231(P-Chem). We thank the Molecular Foundry and Advanced Light Source at Lawrence Berkeley National Laboratory for use of their facilities. We would especially like to thank Dr. Matthew Marcus at the Advanced Light Source and Dr. Shaul Aloni at the Molecular Foundry. We thank Dr. Chong Liu for helpful discussions, and Nigel Becknell and Nick Kornienko for helping run XAS experiments. J.R. gratefully acknowledges the support of the National Science Foundation Graduate Research Fellowship Program (NSF GRFP) under Grant No. DGE-0802270. N.P.D. acknowledges support from the U.S. Department of Energy, Office of Energy Efficiency and Renewable Energy (EERE) Postdoctoral Research Awards under the SunShot Solar Energy Technologies Program.

■ REFERENCES

(1) Dasgupta, N. P.; Sun, J.; Liu, C.; Brittman, S.; Andrews, S.; Lim, J.; Gao, H.; Yan, R.; Yang, P. *Adv. Mater.* **2014**, *26*, 2137.
(2) Liu, C.; Dasgupta, N.; Yang, P. *Chem. Mater.* **2014**, *26*, 415.
(3) Warren, E.; Atwater, H.; Lewis, N. J. *Phys. Chem. C* **2014**, *118*, 747.
(4) Liu, C.; Tang, J.; Chen, H.; Liu, B.; Yang, P. *Nano Lett.* **2013**, *13*, 2989.
(5) Boettcher, S.; Spurgeon, J.; Putnam, M.; Warren, E.; Turner-Evans, D.; Kelzenberg, M.; Maiolo, J.; Atwater, H.; Lewis, N. *Science* **2010**, *327*, 185.
(6) Morales, A. M.; Lieber, C. M. *Science* **1998**, *279*, 208.
(7) Wu, Y.; Yang, P. *J. Am. Chem. Soc.* **2001**, *123*, 3165.
(8) Yang, P.; Lieber, C. M. *Science* **1996**, *273*, 1836.
(9) Trentler, T. J.; Hickman, K. M.; Goel, S. C.; Viano, A. M.; Gibbons, P. C.; Buhro, W. E. *Science* **1995**, *270*, 1791.
(10) Liu, B.; Aydil, E. S. *J. Am. Chem. Soc.* **2009**, *131*, 3985.
(11) George, S. M. *Chem. Rev.* **2010**, *110*, 111.
(12) Dasgupta, N.; Jung, H.; Trejo, O.; McDowell, M.; Hryciw, A.; Brongersma, M.; Sinclair, R.; Prinz, F. *Nano Lett.* **2011**, *11*, 934.
(13) Dasgupta, N.; Liu, C.; Andrews, S.; Prinz, F.; Yang, P. *J. Am. Chem. Soc.* **2013**, *135*, 12932.
(14) Fujishima, A.; Honda, K. *Nature* **1972**, *238*, 37.
(15) Umebayashi, T.; Yamaki, T.; Itoh, H.; Asai, K. *J. Phys. Chem. Solids* **2002**, *63*, 1909.
(16) Liu, G.; Wang, L.; Yang, H. G.; Cheng, H.; Lu, G. Q. *J. Mater. Chem.* **2010**, *20*, 831.
(17) Choi, W.; Termin, A.; Hoffmann, M. *J. Phys. Chem.* **1994**, *98*, 13669.
(18) Garcia-Mota, M.; Vojvodic, A.; Metiu, H.; Man, I. C.; Su, H. Y.; Rossmeisl, J.; Nørskov, J. K. *ChemCatChem* **2011**, *3*, 1607.
(19) Garcia-Mota, M.; Vojvodic, A.; Abild-Pedersen, F.; Nørskov, J. K. *J. Phys. Chem. C* **2013**, *117*, 460.
(20) Liu, B.; Chen, H.; Liu, C.; Andrews, S.; Hahn, C.; Yang, P. *J. Am. Chem. Soc.* **2013**, *135*, 9995.
(21) Newville, M. *J. Synchrotron Radiat.* **2001**, *8*, 96.
(22) Rehr, J. J.; Albers, R. C. *Rev. Mod. Phys.* **2000**, *72*, 621.
(23) Burton, B. B.; Fabreguette, F. H.; George, S. M. *Thin Solid Films* **2009**, 5658.
(24) Pickrahn, K.; Park, S. W.; Gorlin, Y.; Lee, H.; Jaramillo, T.; Bent, S. *Adv. Energy Mater.* **2012**, *2*, 1269.
(25) Strandwitz, N.; Comstock, D.; Grimm, R.; Nichols-Nielander, A. C.; Elam, J.; Lewis, N. *J. Phys. Chem. C* **2013**, *117*, 4931.
(26) Lim, B. S.; Rahtu, A.; Park, J.; Gordon, R. *Inorg. Chem.* **2003**, *42*, 7951.
(27) Lim, B. S.; Rahtu, A.; Gordon, R. *Nat. Mater.* **2003**, *2*, 749.
(28) Au, Y.; Lin, Y.; Kim, H.; Beh, E.; Liu, Y.; Gordon, R. *J. Electrochem. Soc.* **2010**, *157*, 341.
(29) Dicastro, V.; Polzonetti, G. *J. Electron Spectrosc. Relat. Phenom.* **1989**, *48*, 117.
(30) Oku, M.; Hirokawa, K.; Ikeda, S. *J. Electron Spectrosc. Relat. Phenom.* **1975**, *7*, 465.
(31) Gorlin, Y.; Jaramillo, T. *ECS Trans.* **2011**, *41*, 1701.
(32) McCrory, C.; Jung, S.; Peters, J.; Jaramillo, T. *J. Am. Chem. Soc.* **2013**, *135*, 16977.
(33) Man, I.; Su, H.; Calle-Vallejo, F.; Hansen, H.; Martinez, J.; Inoglu, N.; Kitchin, J.; Jaramillo, T.; Nørskov, J.; Rossmeisl, J. *ChemCatChem* **2011**, *3*, 1159.
(34) Gorlin, Y.; Jaramillo, T. *J. Am. Chem. Soc.* **2010**, *132*, 13612.
(35) Su, H.; Gorlin, Y.; Man, I.; Calle-Vallejo, F.; Nørskov, J. K.; Jaramillo, T. F.; Rossmeisl, J. *Phys. Chem. Chem. Phys.* **2012**, *14*, 14010.